


Reentrant prewavy instability in competition between rising and twist modes in ac field-driven electroconvection

Jong-Hoon Huh  and Naoto Miyagawa

Department of Physics and Information Technology, Faculty of Computer Science and Systems Engineering,
Kyushu Institute of Technology, Fukuoka 820-8502, Japan

 (Received 11 March 2021; accepted 17 May 2021; published 3 June 2021)

We report on the prewavy (PW) instability in ac field-driven electrohydrodynamics that is induced in a nematic liquid crystal (NLC) sandwiched between parallel electrodes. The instability is characterized by a twist mode of the NLC director along the vertical orientation to the electrodes (i.e., the z axis), generating a periodic pattern having a large wavelength (λ_{PW}) in the xy plane. The PW periodic to the preferred director \mathbf{n}_0 of the NLC should be distinguished from well-known electroconvection (EC) such as normal rolls (NRs) and abnormal rolls (ARs) with similar wave vectors. A reentrant PW (PW2) was discovered by employing well-adjusted optical conditions and a dynamic image-process method. The wavelength λ_{PW2} of the PW2 accompanying turbulent EC was measured as functions of the applied ac voltage and frequency, which was distinguished from λ_{PW1} of the primary PW (PW1) separated from the NR. Moreover, the appearance, disappearance, and reappearance of the PW were investigated for five frequency regions classified in the ac field-driven EC; it was found that the high frequency and high voltage causes competition between the rising mode (θ , tilting angle to the xy plane) and twist mode (ϕ , in-plane angle to the x axis) of the director through electrohydrodynamic coupling between the director field and flows. We discuss how the PW2 can arise by considering another twist mode known as AR instability.

DOI: [10.1103/PhysRevE.103.062701](https://doi.org/10.1103/PhysRevE.103.062701)

I. INTRODUCTION

Ac field-driven electroconvection (EC) in nematic liquid crystals (NLCs) has been extensively investigated for understanding nonlinear dissipative systems that are out of equilibrium [1–3]. Compared to the Rayleigh-Bénard convection in isotropic fluids, EC provides a rich variety of patterns and dynamics due to anisotropic properties of the NLC [1–4]; in particular, electrohydrodynamic coupling effects between the velocity and director fields often generate unexpected dissipative structures beyond standard theories for EC [5–8]. The electric anisotropy of rodlike molecules of the NLC plays an important role in EC; the director is defined by the locally averaged direction of molecules [i.e., a unit vector \mathbf{n} ($\mathbf{n} \equiv -\mathbf{n}$; $|\mathbf{n}| = 1$)] [5]. In the Carr-Helfrich (CH) mechanism [6], the fundamental EC known as the Williams domain (WD) [7] can be induced by a kind of coupling under an external electric field $\mathbf{E}(t) = (\frac{\sqrt{2}}{d}V)\cos(2\pi ft)\hat{z}$ across a thin-layer NLC (typically, thickness $d = 10 - 100 \mu\text{m}$) between parallel electrodes; fluctuations of the initial director [$\mathbf{n}_0 = (1, 0, 0)$] in thermal noise can be reinforced by a material flow resulting from the Coulomb force acting on space charges that are locally focused by electric anisotropy; when the Coulomb force overcomes the viscoelastic and dielectric restoring force at a critical voltage V_c , an electrohydrodynamic instability arises in the NLC layer. As a result, the WD is optically observed in the xy plane via a lens effect of the periodically modulated director field [$\mathbf{n} = (n_x, 0, n_z)$], showing regular convection rolls (along the y axis) due to a

stationary director field [4,5]. If the ac frequency f exceeds a characteristic frequency f_{cd} , the director \mathbf{n} oscillates in phase with the electric field, generating dielectric rolls due to the oscillating director field in the bulk and accompanying tiny vortices near the electrode surfaces; moreover, the dielectric roll pattern develops into the so-called dielectric chevrons (DCVs) with herringbone structures by increasing V ; therefore, f_{cd} distinguishes the high-frequency dielectric regime ($f > f_{cd}$) from the low-frequency conduction regime ($f < f_{cd}$) [4,5].

Moreover, there exist other characteristic frequencies for the conduction regime ($f < f_{cd}$). First, the Lifshitz frequency f_L was introduced to explain a transition from the oblique rolls (ORs) for $f < f_L$ to the normal rolls (NRs) for $f > f_L$ via breaking the reflection symmetry $x \rightarrow -x$ for the wave vector; thus, the wave vector $\mathbf{k}_{OR}(\parallel \mathbf{n}_0 \parallel \hat{x})$ for the OR can be distinguished from $\mathbf{k}_{NR}(\parallel \mathbf{n}_0)$ for the NR [4,9–11]. Furthermore, it was found that the so-called soft-mode turbulences in the homeotropic configuration [$\mathbf{n}_0 = (0, 0, 1)$] have different underlying mechanisms below and above f_L , respectively [12,13]. Next, a certain characteristic frequency f_{DL} was reported for $f_L < f < f_{cd}$; in experiments, defect lattices (DLs) were generated by an abnormal roll (AR) instability (and skewed varicose modulation) for $f > f_{DL} > f_L$ [14–17]. The AR having $n_y \neq 0$ ($\mathbf{k}_{AR} \parallel \mathbf{n}_0$) can be distinguished from the NR having $n_y = 0$ ($\mathbf{k}_{NR} \parallel \mathbf{n}_0$), breaking the reflection symmetry $x \rightarrow -x$ for the in-plane director \mathbf{n}_{xy} projected in the xy plane; in other words, the AR is induced by the *in-plane rotation of the director*. Accordingly, a *twist mode* $n_{xy} = n_{xy}(z)$

TABLE I. The electric conductivity and dielectric constants of MBBA (at 18 °C) and EBBA (at 35 °C) were measured by using an inductance capacitance impedance (LCZ) meter ($f = 1$ kHz). Although cell 1 to cell 3 were prepared using the same kind of NLC (i.e., MBBA), the values of electric properties were different from one another because of their aging effect (mainly, electrolytic dissociation and recombination) [8,41]. The value of ε_{\perp} of cell 3 abnormally larger than those of cell 1 and cell 2 may be understood by uncontrolled impurity effects [43].

	NLC	$\sigma_{\perp}(\Omega^{-1}\text{m}^{-1})$	ε_{\perp}	$d(\mu\text{m})$
Cell 1	MBBA	1.67×10^{-7}	6.16	50
Cell 2	MBBA	8.37×10^{-8}	6.22	10
Cell 3	MBBA	2.45×10^{-7}	9.11	25
Cell 4	EBBA	0.41×10^{-7}	4.70	25

along the z axis should be considered for the AR in the case of the planar configuration [$\mathbf{n}_0 = (1, 0, 0)$]. Finally, it is known that a prewavy (PW) instability plays an important role in the EC pattern formations for $f > f_w > f_{DL}$ [4,18,19]; this instability is also characterized by the *in-plane rotation of the director*, similar to the AR instability; for the PW, however, no vortex of the fundamental EC (i.e., NR) with a short wavelength ($\lambda \sim d$) is found in the xz plane, but instead, large-scale convection ($\lambda_{PW} \gg d$) is observed in the xy plane together with more complicated flows [18,19]. In particular, the PW instability extends into the high-frequency dielectric regime ($f > f_{cd}$), providing a background pattern for the DCV [4,19]; thus, it is outside the CH theory [5–7].

In this study, we focus on the PW and its relation with various pattern formations. In particular, we show that the PW competes with the usual EC (i.e., NR or AR); as a result, the PW appears, disappears, and reappears due to the competition conditions between the rising and twist modes of the director. Moreover, for five frequency regions for EC, the possibility of *extension of the PW into low-frequency regions* is investigated; notable results that have been overlooked and that could be discovered by a dynamic image-process method are presented.

II. EXPERIMENT

To investigate all frequency regions for EC, four sample cells were prepared by using two typical NLCs [*p*-methoxybenzylidene-*p'*-*n*-butylaniline (MBBA) and *p*-ethoxybenzylidene-*p*-butylaniline (EBBA)]; their important parameters for EC are listed in Table I. The standard shadowgraph method was used for optical observations and measurements [5]. A polarizer (P), analyzer (A), and quarter-wave plate (Q) were used as needed. In this study, $P_{//}$ (parallel to \mathbf{n}_0), A_{\perp} (perpendicular to \mathbf{n}_0), and Q ($\pi/4$ to \mathbf{n}_0) were set as the main optical conditions, and are referred to as $P_{//}QA_{\perp}$ in this paper. Consequently, under the optical condition ($P_{//}QA_{\perp}$), the light propagates successively along the route: light source (PL5761, Philips) $\rightarrow P_{//} \rightarrow$ NLC (sample cell) $\rightarrow Q \rightarrow A_{\perp} \rightarrow$ camera lens. Moreover, different optical conditions, such as $P_{\perp}QA_{\perp}$, $P_{//}A_{\perp}$, and $P_{//}$ only, were replaced if needed. The EC patterns and their dynamics were observed by using computer-controlled image software (SCION IMAGE) and an image-capture board (Scion Corp., PCI-VE5) together

with a charge-coupled device camera (Sony, XC-75) mounted on a polarizing microscope (Meijitech, ML9300); all electro-optical patterns were observed in the xy plane. In particular, a dynamically integrating image-process method (DIIPM) was implemented to improve the resolution of the transmitted light for unusual EC that cannot be visualized in a single image picture; for instance, a picture of an EC pattern was reconstructed in averaged gray scale after integration of 50 frames (with a sampling rate of 3 fps) of a pattern at fixed values of V and f in the adjusted optical conditions; in particular, this method provides crucial evidence for a reentrant PW instability that has been overlooked in past studies [2–5]. In this paper, the reconstructed picture is referred to as a DIIPM image. Measurements for cell 1 to cell 3 (MBBA) and for cell 4 (EBBA) were respectively performed at a fixed temperature of $T = 18$ °C and 35 °C by using an electrothermal control system (TH-99, Japan Hightech). The experimental results in the figures were obtained from cell-1, except for those in Figs. 1, 7, 9, and 10.

III. RESULTS AND DISCUSSION

A. Optical patterns of the PW1

First, we observed optical patterns of the PW in the crossed-nicol (CN) and parallel-nicol (PN) conditions including a quarter-wave plate (Q), as shown in Fig. 1(b); that is, the upper and lower charts of the data and PW patterns were obtained in the $P_{//}QA_{\perp}$ and $P_{\perp}QA_{\perp}$ condition, respectively. From the estimated in-plane angle ϕ with respect to the x axis (see below), we calculated the transmitted optical intensity $I[X(\phi)]$ in an arbitrarily selected line $X(\|\mathbf{n}_0)$ by employing the well-established 2×2 Jones matrix [20,21]:

$$\mathbf{J} = \mathbf{J}_A \times \mathbf{J}_Q \times \mathbf{J}_{NLC} \times \mathbf{J}_P. \quad (1)$$

For instance, in the case of the $P_{//}QA_{\perp}$ condition ($\alpha_P = 0$, $\alpha_A = \pi/2$, $\beta_Q = \pi/4$) in our optical system ($\mathbf{n}_0 \parallel \hat{x}$), each matrix in Eq. (1) is given by

$$\mathbf{J}_P = \frac{1}{2} \begin{bmatrix} 1 + \cos 2\alpha_P & \sin 2\alpha_P \\ \sin 2\alpha_P & 1 - \cos 2\alpha_P \end{bmatrix} = \begin{bmatrix} 1 & 0 \\ 0 & 0 \end{bmatrix}, \quad (2)$$

$$\mathbf{J}_A = \frac{1}{2} \begin{bmatrix} 1 + \cos 2\alpha_A & \sin 2\alpha_A \\ \sin 2\alpha_A & 1 - \cos 2\alpha_A \end{bmatrix} = \begin{bmatrix} 0 & 0 \\ 0 & 1 \end{bmatrix}, \quad (3)$$

$$\begin{aligned} \mathbf{J}_Q &= \begin{bmatrix} \sin^2 \beta_Q + i \cos^2 \beta_Q & \sin \beta_Q \cos \beta_Q (i - 1) \\ \sin \beta_Q \cos \beta_Q (i - 1) & \cos^2 \beta_Q + i \sin^2 \beta_Q \end{bmatrix} \\ &= \frac{1}{2} \begin{bmatrix} 1 + i & i - 1 \\ i - 1 & 1 + i \end{bmatrix}, \end{aligned} \quad (4)$$

where α_P , α_A , and β_Q , respectively, indicate the angles of the polarizer, analyzer, and quarter-wave plate with respect to the x axis. Since the NLC (with thickness d) can be considered as a stack of thin layers, \mathbf{J}_{NLC} for the NLC is described by a summation of the propagation matrix for each slice ($n = 1, 2, \dots, N$):

$$\mathbf{J}_{NLC} = \prod_{n=1}^N \mathbf{P}_n, \quad (5)$$

$$\mathbf{P}_n = e^{i\psi} \begin{bmatrix} \cos \gamma + i \sin \gamma \cos 2\phi_n & i \sin \gamma \sin 2\phi_n \\ i \sin \gamma \sin 2\phi_n & \cos \gamma - i \sin \gamma \cos 2\phi_n \end{bmatrix}. \quad (6)$$

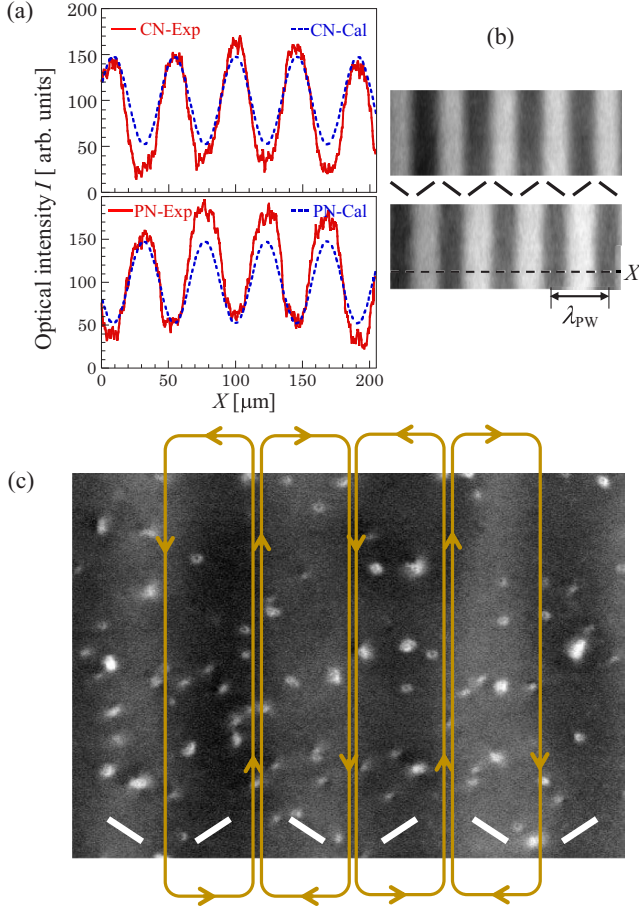


FIG. 1. Transmitted optical intensity $I(X)$ (a) of a prewavy (PW1) (b) obtained in the $P_{//}QA_{\perp}$ [i.e., crossed-nicol (CN), upper] and $P_{\perp}QA_{\perp}$ [i.e., parallel-nicol (PN), lower] conditions, and flows (c) in the PW1 (cell 3) (Supplemental Material [44]); here, P, Q, and A indicate a polarizer, quarter-wave plate, and analyzer, respectively. Moreover, $I(X)$ was calculated by the Jones matrix method, in order to compare with the experimental one that was measured at an arbitrarily selected line (X) in the PW1. The periodic bars in (b,c) indicate the in-plane director \mathbf{n}_{xy} in the midplane of the nematic liquid-crystal cell ($z = d/2$).

Here, ϕ_n , ψ , and γ , respectively, indicate the local in-plane angle, and the retardations of light defined as $\psi = \pi(n_e + n_o)d_n/\lambda_{\text{light}}$ and $\gamma = \pi(n_e - n_o)d_n/\lambda_{\text{light}}$, where n_o and n_e denote the refractive indices of the NLC with respect to the ordinary and extraordinary lights with a wavelength λ_{light} , respectively. In this study, the twisting angle is assumed by $\phi_m(x, z = d/2) = \phi_0 \cos(2\pi x/\lambda_{\text{PW}})$ and $\phi(z) = \phi_m \sin(\pi z/d)$; that is, the intensity $I(x_i)$ was calculated by Eq. (1) at each x_i on X in a PW [Fig. 1(b)], and then $I(x) = I[X(\phi)]$ was obtained by considering the twist configuration, $\phi = \phi(x, z)$, on X . In our calculation, typical values of $n_o = 1.5506$, $n_e = 1.5486$, and $\lambda_{\text{light}} = 650 \times 10^{-3} \mu\text{m}$ were used for $N = 91$ and $d = d_n(N-1) = 25 \mu\text{m}$.

In Fig. 1(a), the calculated intensity $I(X)$ shows good agreement with the experimental one obtained in the line X in the PW [Fig. 1(b)]; in addition, the intensity profile in the $P_{//}QA_{\perp}$ condition (CN) is clearly inverted to that in the $P_{\perp}QA_{\perp}$ condition (PN), both experimentally and numerically.

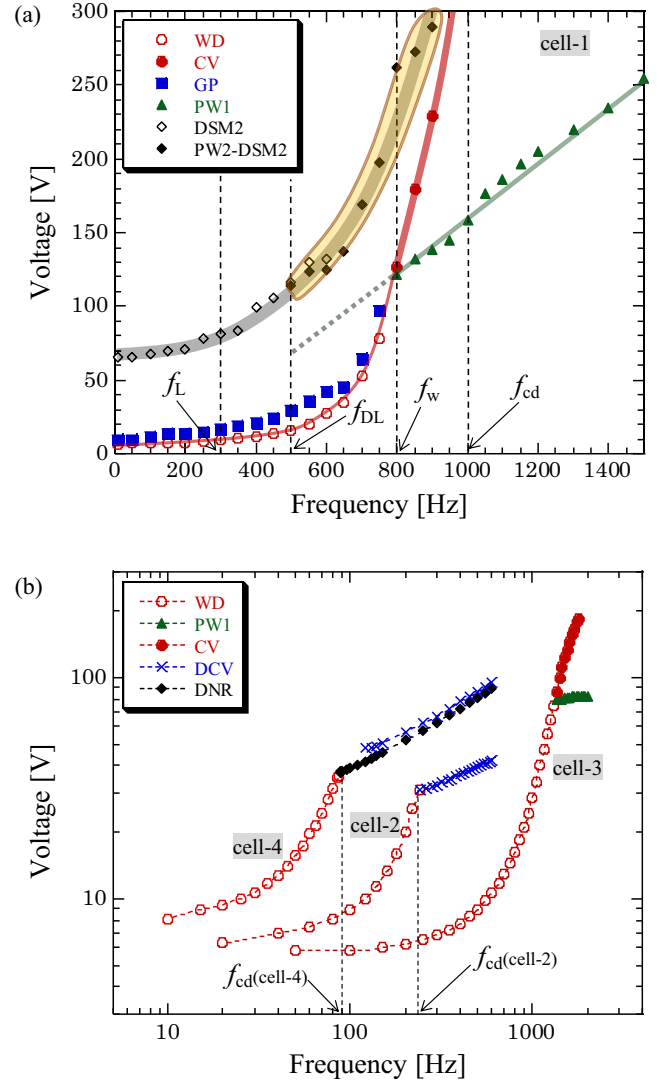


FIG. 2. Phase diagrams in the frequency-voltage plane. (a) Typical thresholds of patterns in cell 1; WD: Williams domain, CV: chevron, GP: grid pattern, PW: prewavy, DSM: dynamic scattering mode. The shaded region for $f_{\text{DL}} < f < f_{\text{cd}}$ indicates coexistence of a PW2 and a DSM2. The dotted thick line between f_{DL} and f_w denotes a presumable threshold line for the PW1 extrapolated from that for $f > f_w$ [4]. (b) Phase diagrams obtained in cell 2, cell 3, and cell 4; DCV: dielectric chevron; DNR: dielectric normal roll. Note that our results were obtained at a fixed $T = 18^\circ\text{C}$ for cell 1 to cell 3 (MBBA) for which the clearing point was almost the same value ($T_c \sim 41^\circ\text{C}$) despite different electric properties as shown in Table I.

In addition, we observed flows in the PW by using a test cell and introducing a small amount of pearl particles (with a diameter of $3 \mu\text{m}$). As shown in Fig. 1(c), the main tracer-particle trajectory shows a large-scale convection ($\lambda_{\text{PW}} \gg d$) in the xy plane [18,19], providing the periodic in-plane director \mathbf{n}_{xy} as seen in Figs. 1(b) and 1(c).

B. Phase diagrams in the frequency-voltage plane

Next, we investigated phase diagrams showing a variety of EC patterns including PWs, as shown in Fig. 2; to examine

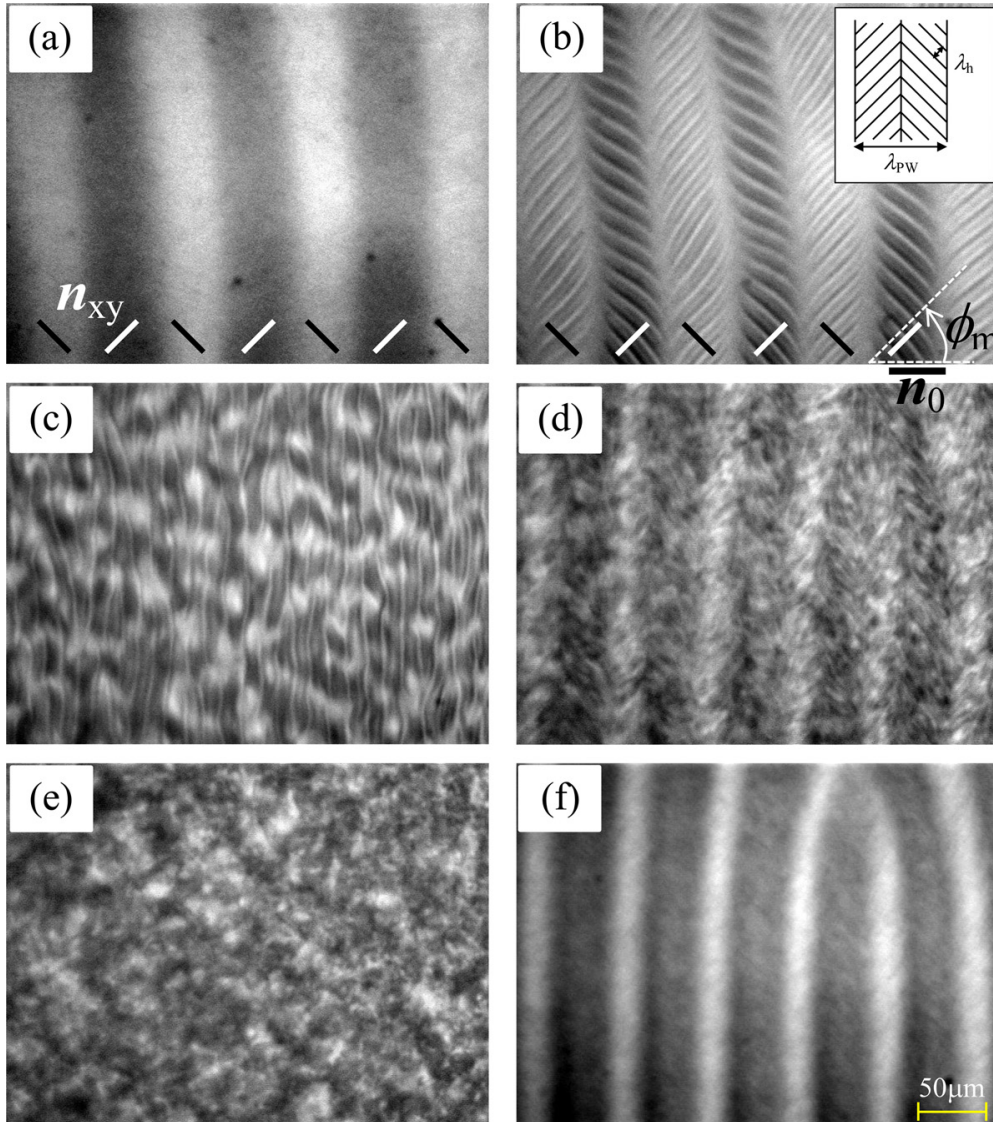


FIG. 3. Appearance of a primary PW (PW1) and a reentrant PW (PW2) ($f = 850 \text{ Hz} > f_w \approx 800 \text{ Hz}$) by increasing $V = 180 \text{ V}$ (a), 201 V (b), 216 V (c), 275 V (d), and 299 V (e); the optical condition was $P_{//}QA_{\perp}$. In particular, (f) is a DIIPM image transformed from (d). The thick bars in (a,b) indicate the in-plane director \mathbf{n}_{xy} ; accordingly, the director field in the midplane ($z = d/2$) determines the maximal twist angle ϕ_m to the initial director $\mathbf{n}_0(\parallel \hat{x})$; in other words, $\pm\phi_m$ corresponds to the counterclockwise- and clockwise-twisted directors, respectively; see also Figs. 6 and 11(d).

all frequency regions ($f < f_{cd}$ and $f > f_{cd}$), the phase diagrams were obtained from four sample cells. In principle, the thresholds V_c of the WD and chevrons (CV) in Fig. 2(a) are safely connected to each other in a smooth curve expected in the CH theory; $V_c \propto (1 + 4\pi^2 f^2 \tau_\sigma^2) / [\zeta^2 - (1 + 4\pi^2 f^2 \tau_\sigma^2)]$ for $f < f_{cd}$, for which τ_σ and ζ denote the charge relaxation time and the Helfrich parameter, respectively [4–6]. However, the CV ($f < f_{cd}$) should be discriminated from the DCV ($f > f_{cd}$) mentioned in Sec. I [4,5,22]. In other words, the thresholds of the WD and CV are fundamental for the primary instability of the CH theory ($f < f_{cd}$), although the patterns are definitely different from each other (see below). On the other hand, the typical EC (i.e., DCV) for $f > f_{cd}$ appears in cell 2 and cell 4, as shown in Fig. 2(b), and the threshold curve $V_c(f)$ is also consistent with that expected in the CH theory; $V_c \propto f^{1/2}$ for $f > f_{cd}$ [4–6].

Note that in Fig. 2(a), there exist two types of PW, a primary PW (PW1) and a reentrant PW (PW2), for $f > f_w$. The PW2 has been found in this study (see below); the PW2 and the dynamic scattering mode (DSM2) were observed separately at times within a small difference of voltages, or at other times both patterns coexisted at certain voltages. Moreover, the threshold line V_{PW1} of the PW1 appears to invade into the *low-frequency region* for $f < f_w$; see the dotted line for $f_{DL} < f < f_w$ (see below). Unfortunately, the PW1 has not yet been explained in the expanded EC theories [23] or in the CH theory [5,6].

In experiments, it is extremely difficult to determine the threshold of the DSM1 [24–26], because the DSM1 cannot be easily differentiated from the highly developed fluctuating WD (FWD) and defect motion dominated turbulence [27]. Thus, the threshold of the DSM2 only is described in Fig. 2(a),

which is distinguishable from DSM1 through a clear optical change [26,28]. In addition, grid patterns (GPs) were observed [24,29–33], in which the density of grids noticeably varied depending on V and f [34]; they are still outside the expanded theories based on the weak nonequilibrium system [5,6,23].

C. Primary PW1 and reentrant PW2

Moreover, we observed the PW1 and PW2 for $f_w < f < f_{cd}$ [Fig. 2(a)] by increasing V . The pattern evolution is shown in Fig. 3. At $V = 175$ V [$\gg V_{PW1} = 129$ V ($f = 850$ Hz)], the (pure) PW1 appears below V_c (CV) [Fig. 3(a)], showing a wavelength λ_{PW1} much larger than λ_{WD} of the WD ($f < f_w$) [19]. With increasing V , a typical CV occurs above V_c (CV) = 180 V [Fig. 3(b)], and successively evolves into an FWD and a DSM1 [e.g., Fig. 3(c)]. Surprisingly, a reentrant PW (i.e., PW2) [Fig. 3(d)] appears just before developing into a DSM2 [Fig. 3(e)]. Note that at fixed values of $f = 850$ Hz and $V = 275$ V, the PW2 [Fig. 3(d)] could be clearly visualized in its DIIPM image [Fig. 3(f)]; since the fast fluctuations of the transmitted optical intensity resulting from turbulent EC became smooth in the DIIPM, the almost time-independent PW2 could be reconstructed. Conventional observations under the $P_{//}A_{\perp}$ or $P_{//}$ condition fail to obtain the PW1 and PW2 [20]. Under the additional quarter-wave plate (i.e., $P_{//}QA_{\perp}$), the periodic stripes of the PW1 (without EC) and PW2 (with turbulent EC) could be visualized. As the transmitted optical intensity of the PW1 was inverted in the $P_{\perp}QA_{\perp}$ condition (Fig. 1), that of the PW2 [Fig. 3(f)] was also inverted for the same reason. These results indicate that the PW1 and PW2 originate from the breaking of degeneracy of the clockwise- and counterclockwise-twisted directors [17].

Furthermore, considering the wave vector \mathbf{k}_{NR} of the NR (i.e., $\mathbf{k}_{NR} \parallel \mathbf{n}_0$), the clockwise- and counterclockwise-twisted directors $\mathbf{n}_{xy}(z = d/2)$ are estimated as black and white bars in Figs. 3(a) and 3(b), respectively. In other words, the in-plane angle $\phi(z)$ for the twist mode along the z axis can be estimated by assuming $\phi(z) = \phi_m \sin(\pi z/d)$, as depicted in Figs. 3(a) and 3(b). In addition, the maximal angles ϕ_m of the twist modes in the midplane ($z = d/2$) can be measured as finite values between \mathbf{n}_{xy} and $\mathbf{n}_0(\parallel \hat{x})$; e.g., $\phi_m \approx \pm \pi/4$ in Figs. 3(a) and 3(b), which is consistent with the saturation angle $\phi_{sat} \approx \pm \pi/4$ of the PW1 reported in the previous study [18]; note that ϕ_m can be easily estimated by considering the constraint condition of the NR, i.e., $\mathbf{k}_{NR} \parallel \mathbf{n}_0$; indeed, $\mathbf{k}_{NR} \parallel \mathbf{n}_{xy}(z = d/2)$ in the present case [35].

Obviously, Fig. 4(a) shows that both PWs (i.e., PW1 and PW2) may originate from the same cause (i.e., the twist mode); thus, the wavelength λ_{PW1} of the PW1 is connected with λ_{PW2} of the PW2 via the CV and DSM1 by a linear interpolation; no data are found between $V \approx 210$ and 250 V, because of the collapse of the CV [Fig. 3(c)]. Moreover, it is found that the decreasing rate (i.e., the slope) of $\lambda_{PW1}(V)$ is different from that of $\lambda_{PW2}(V)$; the latter coupling to an EC mode (i.e., NR or AR) is slower than the former separated from it:

$$\lambda_{PW1} \propto a_1 V, \quad (7)$$

$$\lambda_{PW2} \propto a_2 V, \quad (8)$$

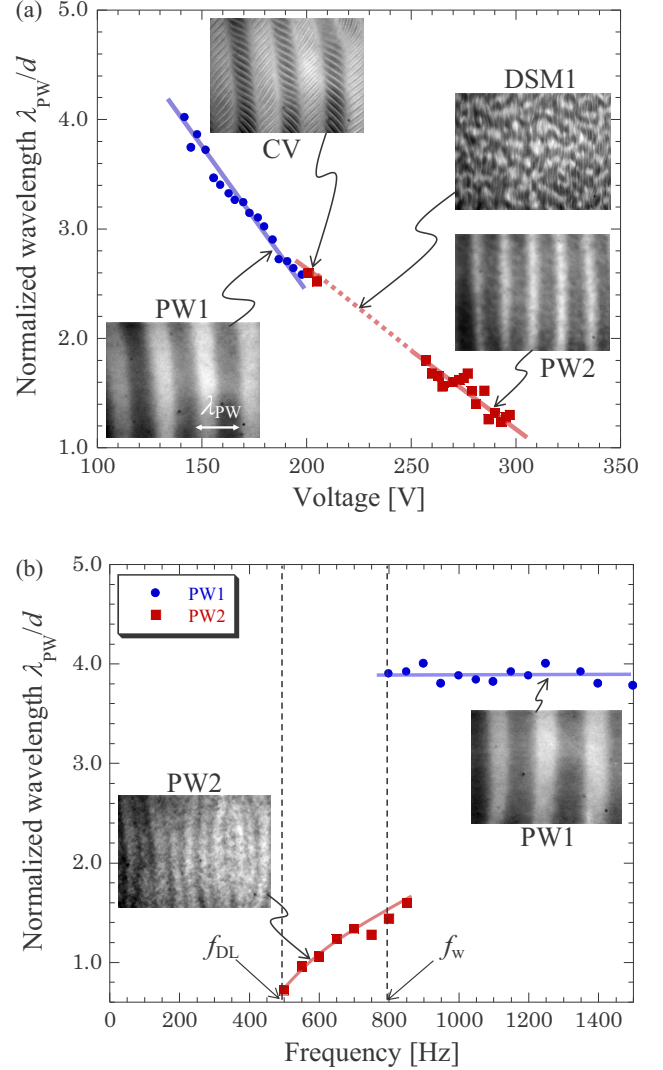


FIG. 4. Wavelength λ_{PW} of the PW1 and PW2 as a function of the ac voltage V ($f = 850$ Hz $> f_w \approx 800$ Hz) (a), and as a function of the ac frequency f [$\varepsilon_{PW} = (V^2 - V_{PW1}^2)/V_{PW1}^2 \approx 0.1$ for the PW1 and $\varepsilon_{PW2} = (V^2 - V_{PW2}^2)/V_{PW2}^2 \approx 0.1$ for the PW2] (b). All pictures were obtained in the $P_{//}QA_{\perp}$ condition; the PW2 in (a) is a DIIPM image. Note that the dotted line in (a) does not provide the wavelength because of collapse of the PW1; moreover, the two slopes of $\lambda_{PW}(V)/d$ are different from each other, indicating different decreasing rates of the wavelengths.

where $a_1 = -1.33 \times 10^{-6} \text{ mV}^{-1}$ and $a_2 = -0.727 \times 10^{-6} \text{ mV}^{-1}$ ($|a_1| > |a_2|$). Furthermore, the difference of the wavelengths is definitely exhibited as a function of f , as shown in Fig. 4(b); λ_{PW1} has no dependence on f , whereas λ_{PW2} is characterized by f dependence showing a monotonic increase:

$$\lambda_{PW1} \approx b_1 d, \quad (9)$$

$$\lambda_{PW2} \propto \left(\frac{f - f_{DL}}{f_{DL}} \right)^{\delta}, \quad (10)$$

where $b_1 = 3.89$ and $\delta = 0.656$ ($f_{DL} \approx 500$ Hz in cell 1). Accordingly, the EC (i.e., NR or AR) is important to form

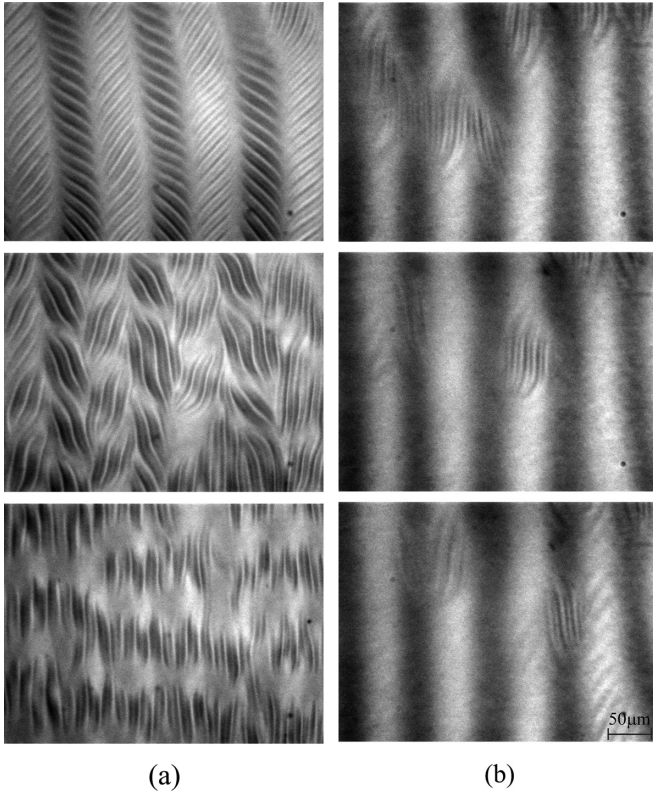


FIG. 5. (a) A transient CV changing into defect chaos with the elapse of time [top: 1 s after applying $V = 201$ V ($f = 850$ Hz $< f_w \approx 800$ Hz) $> V_c = 182$ V; middle: 5 s; and bottom: 20 s]. (b) Appearance and disappearance of localized EC (i.e., NR) in the PW1 with the elapse of time (top: 1 s after applying $V \approx V_c$; middle: 3 s; and bottom: 5 s).

the structure of the PW2, because λ_{NR} and V_c are sensitive to f [4,5].

In particular, the collapse of the CV and the appearance of the PW2 indicate that in the midst of coupling between the n_{xz} mode (and the velocity v_{xz}) for the EC and the n_{xy} mode (and v_{xy}) for the PW (Fig. 1), the two modes may compete with each other, and then the PW becomes alive (PW2) or suppressed (DSM1 and DSM2). In fact, the CV [Fig. 3(b)] indicating a kind of coexistence of a PW1 and an NR was unstable, as shown in Fig. 5; a PW1 in the EC (i.e., NR) by increasing V is destabilized, and then vanishes within 5–10 s, providing defect-dominant EC such as an FWD or a DSM1 [Fig. 5(a), and also Fig. 3(c)]. On the other hand, Fig. 5(b) shows that at extremely near V_c (CV) = 182 V, the PW1 and the NR coexist for a relatively long time ($\gg 10$ s) with changing NR-occupied spaces randomly; the irregular appearance and disappearance of the NR indicate sensitive competition of the director and velocity fields between the two modes in uncontrolled conditions such as irregular thermal fluctuations and impurity effects accompanying flows.

D. Extension of the PW1 threshold line into low frequencies

In general, owing to $V_{PW1} = V_{PW1}(f > f_w)$, the PW1 can be a background pattern of the CV for $f_w < f < f_{cd}$ [Fig. 2]

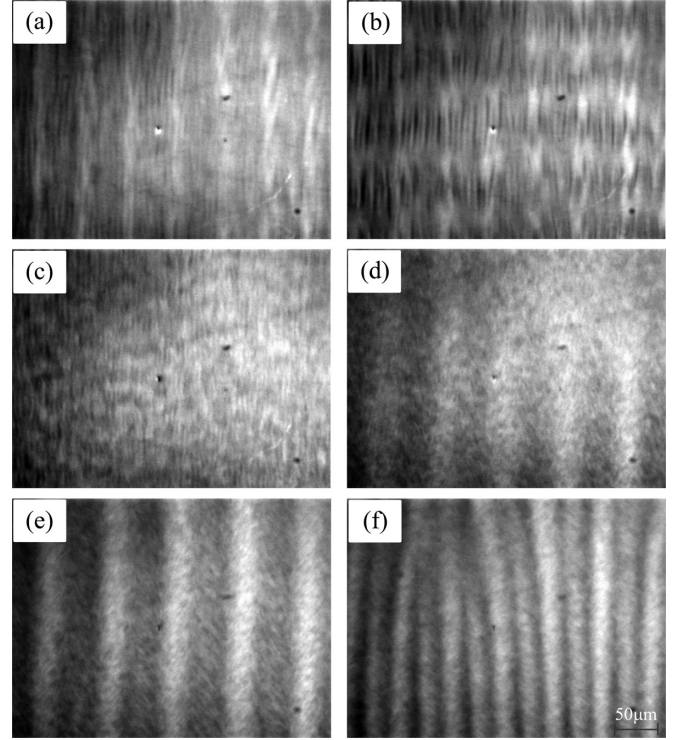


FIG. 6. Pattern evolution ($f_{DL} < f = 600$ Hz $< f_w$) by increasing $V = 80$ V (a), 86 V (b), 122 V (c), 124 V (d), 129 V (e), and 146 V (f). All pictures are DIIPM images obtained in the $P_{//}QA_{\perp}$ condition. A defect-lattice (DL) pattern is well visualized in (a,b). A PW1 hidden in the (usual) $P_{//}$ condition is revealed in (d), which is more clearly visualized in (e,f) as its wavelength decreases; see also Figs. 3 and 11(c).

[18,19], and also of the DCV for $f > f_{cd}$; in other words, no limitation of high frequencies for the PW1 appears to exist ($f > f_w$). Thus, the PW1 is separately observed without coupling to other modes below V_c (CV and DCV). However, there exists a possibility of the PW1 threshold line [i.e., $V_{PW1}(f)$] extending into low-frequency regions ($f < f_w$), as shown in Fig. 2(a); note the dotted line for $f_{DL} < f < f_w$ [4]. In fact, the DL is known to exist in this frequency region, independent of the PW [11,36,37]. By using the DIIPM, we found evidence of the PW1 that would be induced at the dotted line, as shown in Fig. 6. Although the stable PW1 was not observed directly because of suppression by the EC (i.e., DL), the PW2 [Fig. 6(d)] following a DL [Figs. 6(a) and 6(b)] and a DSM1 [Fig. 6(c)] could be observed; by increasing V , the PW2 is more clearly visualized and its wavelength λ_{PW2} decreases [Figs. 6(d)–6(f)]. Eventually, it became the PW2 that is indistinguishable from that for $f > f_w$; in this case, the PW1 and PW2 do not need to be classified, because the PW1 separated from EC is not observed (i.e., $V_{PW} > V_c$). Unlike the PW for $f > f_w$ (Fig. 3), this PW was relatively stable and remained alive for a long time ($\gg 10$ s). In previous studies [18,19,22], the conventional optical condition and image processing were not able to differentiate Figs. 6(c)–6(f) from one another; note that all pictures in Fig. 6 are DIIPM images obtained in the $P_{//}QA_{\perp}$ condition.

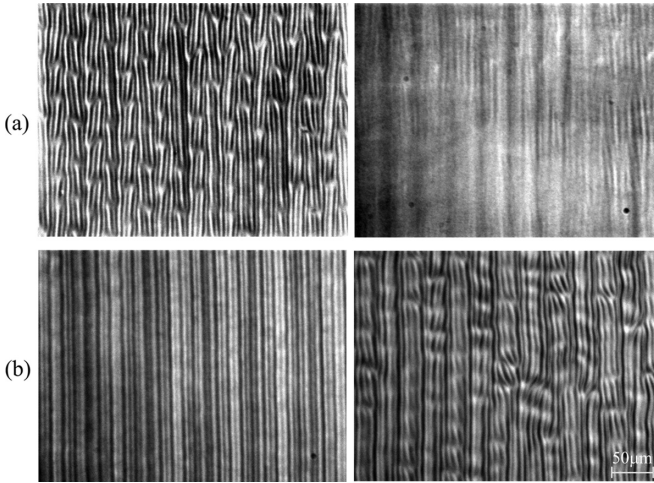


FIG. 7. (a) A DL pattern in the $P_{//}$ condition (left) and $P_{//}QA_{\perp}$ condition (right) in cell 3 ($V = 65$ V and $f = 1200$ Hz $< f_w \approx 1300$ Hz). (b) An abnormal roll (AR) pattern at $V = 19$ V (left) and an immature DL at $V = 21$ V (right) in the same $P_{//}$ condition in cell 2 ($f = 150$ Hz $< f_w \approx 245$ Hz).

On the other hand, for different cells (cell 2 and cell 3) having different d , such a PW2 [Figs. 6(d)–6(f)] was not observed in this frequency region ($f < f_w$), but the AR occurred as a different n_{xy} mode. Figure 7 shows a DL [Fig. 7(a)] in cell 2 and an immature DL [Fig. 7(b)] in cell 3, which were formed on the background of the AR; that is, under different optical conditions [Fig. 7(a)], a DL (left-hand picture) and an AR (right-hand picture) were clearly observed at fixed values ($V = 65$ V and $f = 1200$ Hz) under the $P_{//}$ and $P_{\perp}QA_{\perp}$ conditions, respectively; furthermore, under the fixed $P_{//}$ condition [Fig. 7(b)], an AR (left-hand picture) and an immature DL (right-hand picture) were obtained at different values $V = 19$ and 21 V ($f = 150$ Hz), respectively. These results imply that the n_{xy} modes (i.e., PW or AR) sensitively depend on d (i.e., the volume of bulk); intuitively, the twist mode of the PW2 along the d direction (i.e., the z axis) may be induced more easily in cell 1 ($d = 50$ μ m) than in cell 2 ($d = 10$ μ m) and cell 3 ($d = 25$ μ m), although the well-known Fréedericksz transition voltage $V_F = \pi\sqrt{K_2/(\epsilon_0\Delta\epsilon)}$ for the twist mode is independent of d if $\phi_m \ll 1$ near V_F [5]. Conclusively, for appropriate conditions including d , the PW1 and PW2 can be found for $f_{DL} < f < f_w$. However, the possibility of the extension of the threshold line of V_{PW1} for cell 2 and cell 3 still remains, requiring more sophisticated experimental approaches; that is, a systematic investigation on the d dependence of V_{PW1} is needed with highly sensitive optical observations and image processing to enable the measurement of small in-plane angles ($\phi_m \ll 1$).

E. Pattern evolutions for other frequency regions

Finally, for much lower-frequency regions ($f < f_{DL}$), the pattern formations were examined, expecting the appearance of the PWs. Figure 8(a) shows a typical pattern evolution for $f_L < f < f_{DL}$. With increasing V , an NR appears at V_c , and then evolves into a GP at its threshold voltage V_{GP} ($>$

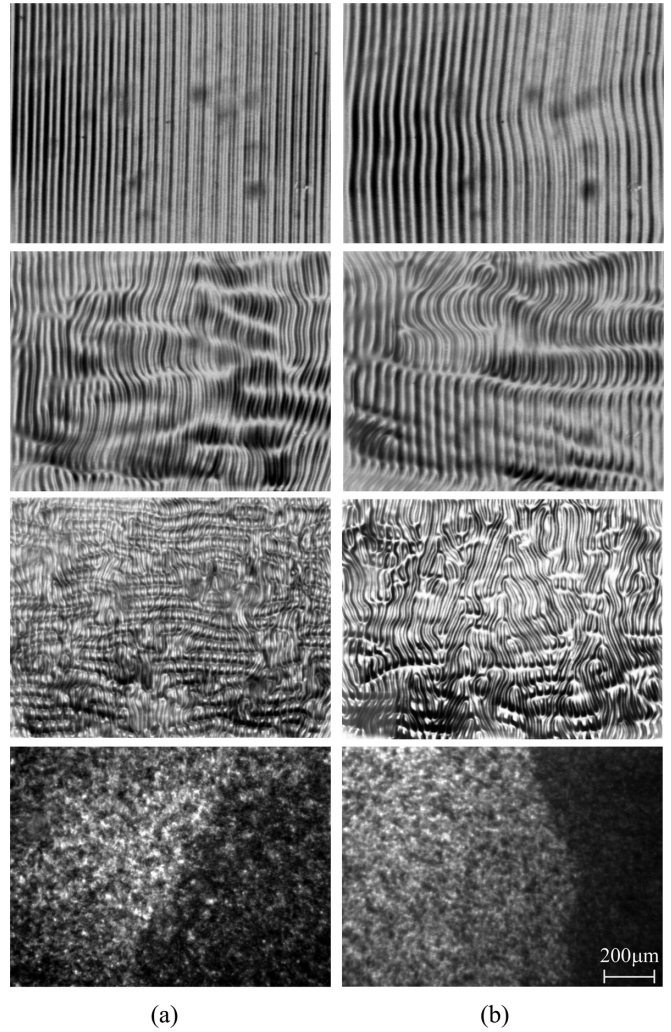


FIG. 8. Pattern evolution (a) for the normal roll (NR) region ($f = 450$ Hz $> f_L \approx 300$ Hz) by increasing V from 15 to 112 V (from upper to lower), and (b) for the oblique roll (OR) region ($f = 100$ Hz $< f_L$) by increasing V from 7.1 to 68 V (from upper to lower). The DSM1 (left) and DSM2 (right) coexist in the turbulent patterns in the lowest row, which are optically distinguished from each other. There is no evidence of the PW. All pictures were observed in the $P_{//}$ condition.

V_c) through defect motions and skewed varicose modulations [24,32–34]; eventually, the GP develops into a DSM2 via a DSM1 [24]. No evidence of the existence of the PW1 and PW2 was found in the $P_{//}QA_{\perp}$ as well as the single $P_{//}$ condition, unlike the region for $f_{DL} < f < f_w$; that is, the estimated threshold line of V_{PW1} appears to be cut off at $f \sim f_{DL}$. In addition, note that the GP is most regularly formed at appropriate f and V ; e.g., see the picture in the third row of Fig. 8(a). The density ρ_{GP} of the grid cell in the GP has a maximal value at a certain f and V [34]. Very recently, such an interesting pattern formation for the GP including complicated $n_{xz}(x, y)$ and frozen defects has been reported [34]. For the OR region ($f < f_L$), moreover, Fig. 8(b) shows a typical pattern evolution in the increase of V ; an OR successively evolves into a DSM2, similar to that for the NR ($f_L < f < f_{DL}$), but does not form the typical GP having a sufficient grid density (above

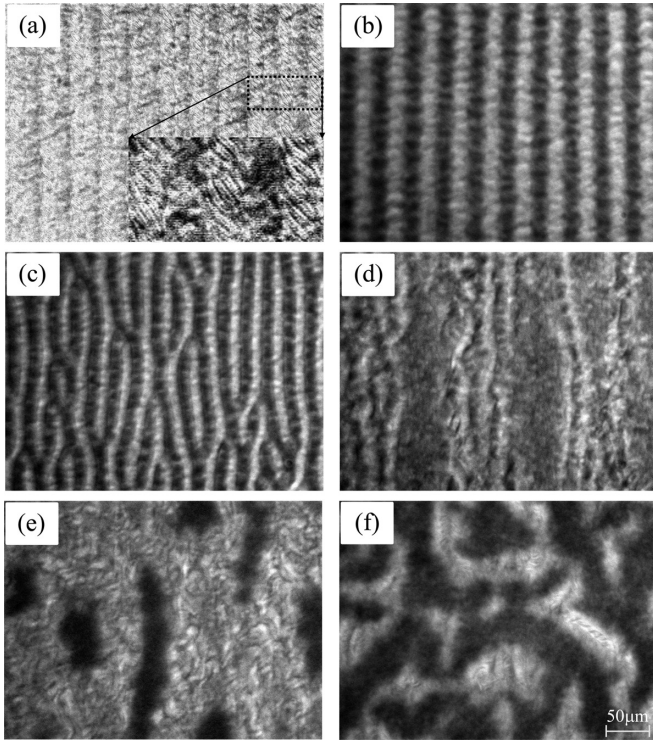


FIG. 9. Pattern evolution ($f = 300 \text{ Hz} > f_{cd} \approx 245 \text{ Hz}$ in cell 2) by increasing $V = 24 \text{ V}$ (a,b), 41 V (c), 48 V (d), 53 V (e), and 60 V (f). (a) was obtained in the $P_{//}QA_{\perp}$ condition. A PW1 appears as a background pattern of a DCV near V_c , and the PW1 and DCV are perceivable in (a). The PW1 (b) develops into a complicated pattern as its wavelength decreases (c) and collapses by turbulent EC invading the periodic PW bands (i.e., clockwise- and counterclockwise-twisted director fields) (d); for higher V , turbulent EC showing the DSM1 (gray) and DSM2 (black) is generated (e) and becomes complicated (f).

40% in the whole image) [34]. No evidence of the existence of the PW1 and PW2 was found in this lowest-frequency region either.

On the other hand, for the typical high-frequency dielectric region ($f > f_{cd}$), the PW1 and PW2 were examined by using

cell 2 in which the DCV arose as a primary instability at V_c ; see also Fig. 2(b). It is found in cell 2 that the PW threshold V_{PW1} appears to be overlapped with V_c ; thus, the DCV is formed at $V_c (= V_{PW1})$ as a combination pattern of dielectric normal rolls (DNRs) and a PW. Such a pattern evolution is shown in Fig. 9 [38]; both the PW1 and DCV have a low optical resolution in the $P_{//}$ condition [Fig. 9(a)] but the PW1 has a high optical resolution in the $P_{//}QA_{\perp}$ condition [Fig. 9(b)]. In the $P_{//}QA_{\perp}$ condition, it is found that the PW1 [Fig. 9(b)] evolves into complicated turbulence [Fig. 9(d)] with decreasing λ_{PW1} [Fig. 9(c)] and, finally, it goes into developed turbulence (i.e., DSM2) with the DSM2 slowly expanding into the DSM1 region [Figs. 9(e) and 9(f)]. The reentrant PW2 as in Fig. 3(d) is not found, since the comparable competition (for $f_{DL} < f < f_{cd}$) may be not realized by the oscillation of the director in this dielectric region ($f > f_{cd}$) [5].

Moreover, if V_{PW1} is placed above V_c (DCV) because of unknown conditions of EC cells [38], the DNR (i.e., prechevrons) arises as a primary instability, and then the DCV follows it [20,38]; such a DNR-developed DCV (DCV1) was found in cell 4 [Fig. 2(b)], as shown in Fig. 10(a). The wide striped domains in the DCV1 may be induced by the defect-mediated in-plane director modulation [20,38], which should be differentiated from the PW instability. DCV ($f > f_{cd}$) can be induced before PW [$V_c(\text{DCV}) < V_{PW}$] and after PW [$V_c(\text{DCV}) > V_{PW}$]. Accordingly, the PW-originated DCV (DCV2) [Fig. 10(b)] above V_{PW} can be distinguished from the DCV1 [Fig. 10(b)] [38]. However, the twisting director modulations in both DCVs providing wide striped domains in the $P_{//}QA_{\perp}$ condition (Fig. 10) cannot be distinguished from each other. In addition, note that the defect-free CV [Fig. 3(b)] is distinguishable from the DCV1 [Fig. 10(a)] and DCV2 [Fig. 10(b)]. The CV originates from a combination of the PW and NR in the bulk of the cell, whereas the DCV1 does so from a combination of the DNR and defects due to oscillating n_{xz} and secondarily induced n_{xy} director modulations [5] in bulk or near the surface of the cell [39]; the DCV2 originates from a combination of the PW and the DNR (and defects) [38]. As a result, the wavelength λ_h of the herringbone structure in the DCV1 and DCV2 ($f > f_{cd}$) is much smaller than that in the CV ($f < f_{cd}$) in Fig. 3(b) [22,40].

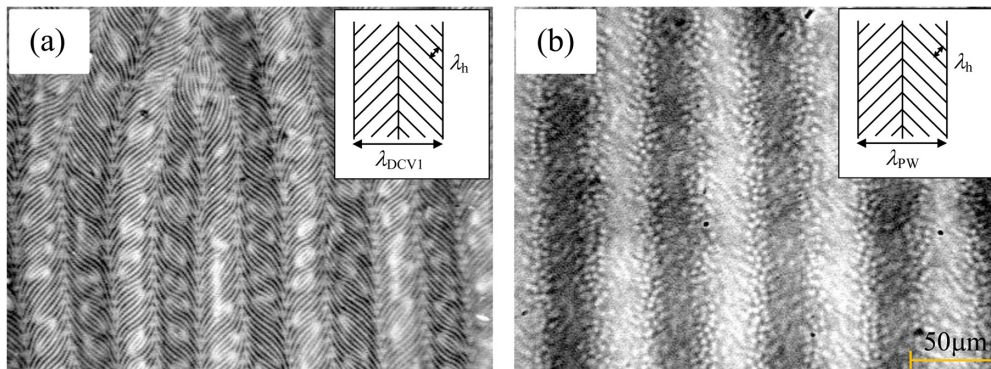


FIG. 10. (a) A DNR-developed DCV (DCV1) observed at $f = 250 \text{ Hz} (> f_{cd} \approx 90 \text{ Hz}$ in cell 4) and (b) A PW-originated DCV (DCV2) observed at $f = 2000 \text{ Hz} (> f_{cd} \approx 1400 \text{ Hz}$ in a cell); see cell 4 (MBBA:EBBA = 50:50 in wt %) in Ref. [38]. Both DCVs were observed in the $P_{//}QA_{\perp}$ conditions. Note that the wide striped domains in both DCVs are indistinguishable from each other although they have completely different origins; those of DCV1 originate from twisting modulation of the director via generation of defects, whereas those of DCV2 are induced by the PW instability providing the twisting modulation.

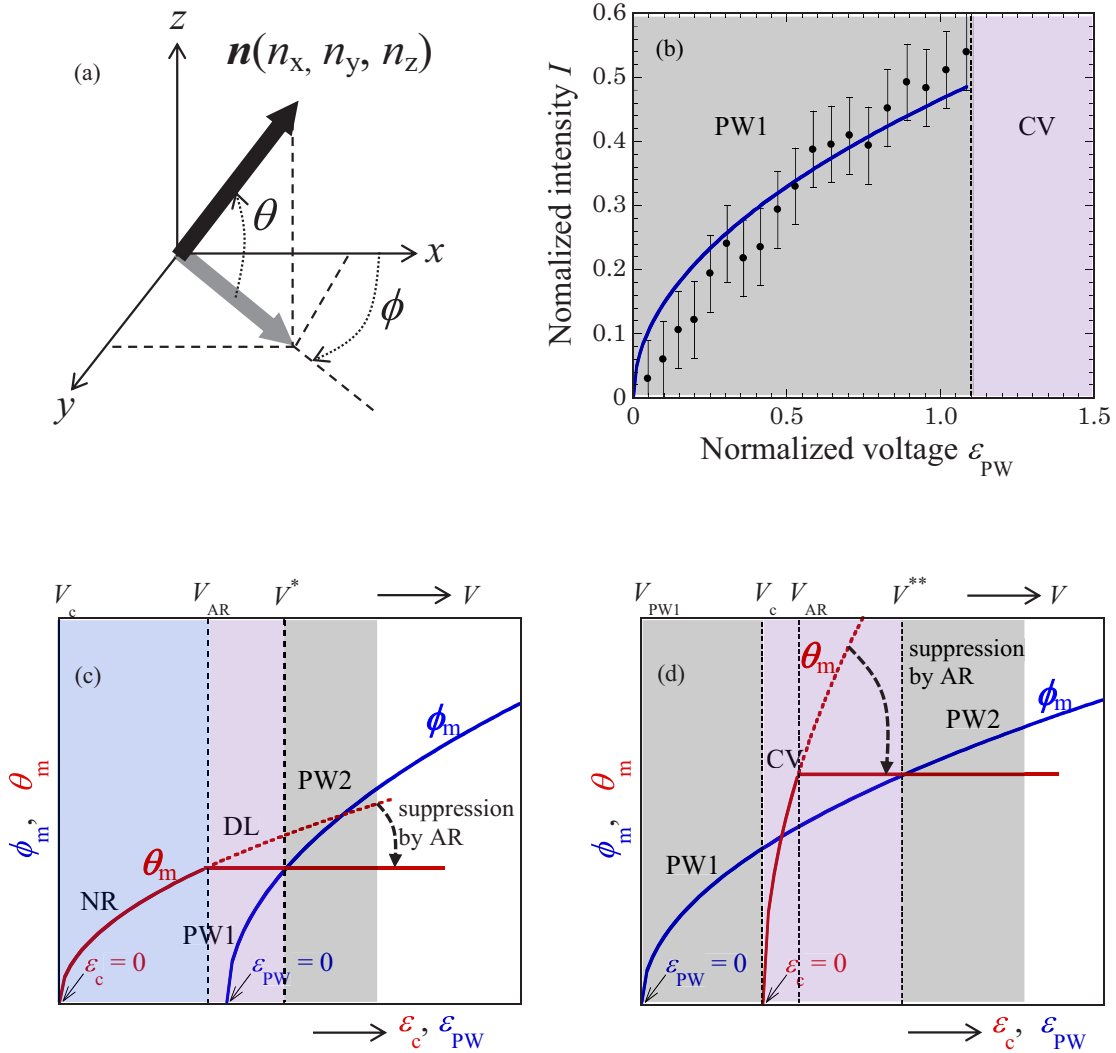


FIG. 11. A possible mechanism for the appearance of the PW1 and PW2. (a) The director \mathbf{n} in EC having a twist mode (ϕ) as well as a rising mode (θ); (b) normalized (transmitted optical) intensity I of the PW1, $I \propto \phi_m = c_\phi \sqrt{\epsilon_{PW}}$; (c) appearance of the PW2 in the case of $f_{DL} < f < f_w$; and (d) appearance of the PW1 and PW2 in the case of $f_w < f < f_{cd}$. The PW1 cannot be observed because of the suppression by a DL on it for $f_{DL} < f < f_w$ (c), whereas it can occur with the PW2 because of $V_{PW1} < V_c$ for $f_w < f < f_{cd}$ (d). See also Figs. 3 and 6.

F. Possible mechanism for the reentrant PW2

In this study, the PW1 and PW2 were successfully observed and classified for $f < f_w$ and $f > f_w$ by using our optical method and image processing. By taking into account the appearance of the PW1 and PW2, a possible underlying mechanism for the PW2 by the competition between the EC (i.e., NR or AR) and PW1 is described as follows.

In principle, EC patterns are characterized by the rising angle θ and twist angle ϕ of the (representative) director [Fig. 11(a)]; the angles had already been examined for the PW1 [18] as well as the NR and AR [17]. For the PW1, the transmitted light intensity I proportional to $\phi_m(z = d/2)$ was checked as a function of $\epsilon_{PW} = (V^2 - V_{PW1}^2)/V_{PW1}^2$, as shown in Fig. 11(b); $I \propto \phi_m \propto \sqrt{\epsilon_{PW}}$ for $\phi_m < \pi/4$ [18,20].

As seen in Fig. 11(c), for $f_{DL} < f < f_w$, θ_m is first induced at $\epsilon_c = (V^2 - V_c^2)/V_c^2 = 0$ (i.e., $V = V_c$) and increases as $\theta_m = c_\theta \sqrt{\epsilon_c}$, and then, ϕ_m is induced at $\sqrt{\epsilon_{PW}} = 0$ (i.e.,

$V_{PW1} > V_c$) and increases as $\phi_m = c_\phi \sqrt{\epsilon_{PW}}$; usually, $c_\theta \neq c_\phi$. Moreover, it should be considered that θ_m saturates at a finite value because of the appearance of the AR instability with another twist angle ϕ'_m [17]. Assuming that the ϕ mode is active if $\phi_m > \theta_m$, the NR ($\theta_m > \phi_m = 0$) appears below V_{PW1} (i.e., $\epsilon_{PW} = 0$), and the DL [$\theta_m > \phi_m \neq 0$ (or $\theta_m \neq 0$; $\phi'_m \neq 0$)] arises above V_{AR} ; then the PW2 ($\phi_m > \theta_m$) appears at V^* , although V is high intensity, close to that for the DSM1. Finally, the DSM2 randomizes both the θ and ϕ modes at sufficiently higher voltages ($V \gg V^*$). Since the PW1 ($\phi_m < \theta_m$) is suppressed by the DL ($V < V^*$), it does not occur for $f_{DL} < f < f_w$. Note that the suppression of the rising mode (θ) by the AR is crucial for the appearance of the PW2 [Fig. 11(c)] before the occurrence of the DSM2. This well explains the experimental result in Figs. 2(a) and 6. In the same way, for $f_w < f < f_{cd}$ [Fig. 11(d)], the PW1 ($\phi_m > \theta_m = 0$) appears for $V_{PW1} < V < V_c$ and it reenters the PW2 ($\phi_m > \theta_m$) for $V > V^{**}$ via the FWD or DSM1 ($\theta_m > \phi_m$) after a

transient CV. The AR instability also plays a crucial role in this pattern evolution; see the experimental result in Figs. 2(a) and 3.

Unfortunately, however, the underlying mechanism of the PW1 is not yet known, although experimental reports showed the director and velocity fields [18,19]. For future studies on the mechanism of the PW1, it is worth mentioning its features in comparison with the AR having a similar twist mode: (1) The PW1 has a definite wavelength $\lambda_{\text{PW1}} (\gg d)$, whereas the AR does not. (2) The PW1 is independent of the normal EC (i.e., NR), whereas the AR is induced by the destabilization of the NR; therefore, the PW1 is due to pure n_x and n_y components, but the AR has $n_z (\neq 0)$ as well as n_x and n_y components. (3) The PW1 has no limitation of high frequencies; e.g., the PW1 was observed up to at least 50 kHz ($f \gg f_{\text{cd}}$) in cell 3 [Fig. 2(b)], whereas the AR is limited by the cutoff frequency f_{cd} . That is, the AR belongs to the low-frequency conduction regime ($f < f_{\text{cd}}$), but the PW1 does not depend on the typical regimes ($f < f_{\text{cd}}$ and $f > f_{\text{cd}}$) although it appears to have a minimal frequency for its occurrence ($f > f_{\text{DL}}$ in this study).

Finally, it is also worth noting similar instabilities previously found in high frequencies ($f > f_w$ or $f > f_{\text{cd}}$) [5]. Although they show similar threshold behavior with respect to the ac frequency, their wavelengths are quite different from one another: (1) The isotropic mode (or electrolyte mode) has f dependence on the wavelength [5], whereas the PW1 mode has no such f dependence [Fig. 4(b)]. (2) The inertia mode has a smaller wavelength ($\sim d$) than the PW1 mode ($\lambda_{\text{PW1}} \sim 4d$) [Fig. 4(b)]; however, it has similar flows in the xy plane that are observed in the PW1 mode [Fig. 1(c)] [5,40,42]; also see the Supplemental Material [44]. More detailed investigation is needed to differentiate one from the other, or to unify them beyond the differences.

IV. SUMMARY AND CONCLUSION

The appearance, disappearance, and reappearance of the PW have been investigated in all frequency regions for ac field-driven EC. We have discovered a reentrant PW (PW2) in two high-frequency regions at which one usually expects developed EC such as the FWD, DL, or turbulent states (i.e., DSM1 and DSM2). In particular, by employing well-adjusted optical conditions and dynamic image processing, the PW2 could be differentiated from the developed EC. Obviously, the PW2 as well as the primary PW1 is a kind of twist mode; moreover, the wavelength of the PW2 is different from that of the PW1 in the functions of the ac voltage and frequency. Furthermore, the extension of the threshold line of the PW1 into the low-frequency region has been clarified [4]. Due to the conventional optical conditions and limited image-processing methods, these significant results had been overlooked to date. From our experimental results, we propose a possible mechanism for the appearance of the PW2: The competition between the rising mode (θ) and twist mode (ϕ) of the director is important to the pattern formation and evolution including the PWs; in particular, the suppression of the θ mode by the AR instability plays a crucial role in this mechanism. As a result, the appearance of the twist mode of the PW having a spatial periodicity provides a variety of dissipative structures such as the CV and DCV in planarly aligned cells (in this study), and wavy patterns and spiral wavy patterns in homeotropically aligned cells [22,24]. In a future study, similar instabilities, such as isotropic mode and inertia mode, should be clarified in comparison with the present PW instability.

ACKNOWLEDGMENT

This work was supported by JSPS KAKENHI Grant No. 18K03464.

-
- [1] M. C. Cross and P. C. Hohenberg, *Rev. Mod. Phys.* **65**, 851 (1993).
 - [2] S. Kai, *Pattern Formation in Complex Dissipative Systems* (World Scientific, London, 1991).
 - [3] See reviews and references, e.g., T. John, J. Heuer, and R. Stannarius, *Phys. Rev. E* **71**, 056307 (2005); A. Buka, N. Eber, W. Pesch, and L. Kramer, *Phys. Rep.* **448**, 115 (2007).
 - [4] N. Eber, P. Salamon, and A. Buka, *Liq. Cryst. Rev.* **4**, 101 (2016).
 - [5] L. M. Blinov and V. G. Chigrinov, *Electrooptical Effects in Liquid Crystal Materials* (Springer, New York, 1994).
 - [6] E. F. Carr, *Mol. Cryst.* **7**, 253 (1963); W. Helfrich, *J. Chem. Phys.* **51**, 4092 (1969).
 - [7] R. Williams, *J. Chem. Phys.* **39**, 384 (1963).
 - [8] R. Ribotta, A. Joets, and L. Lei, *Phys. Rev. Lett.* **56**, 1595 (1986); **56**, 2335(E) (1986).
 - [9] W. Zimmermann and L. Kramer, *Phys. Rev. Lett.* **55**, 402 (1985).
 - [10] M. Dennin, D. S. Cannell, and G. Ahlers, *Phys. Rev. E* **57**, 638 (1998).
 - [11] D. Funfschilling, B. Sammulu, and M. Dennin, *Phys. Rev. E* **67**, 016207 (2003).
 - [12] Y. Hidaka, J.-H. Huh, K.-I. Hayashi, S. Kai, and M. I. Tribelsky, *Phys. Rev. E* **56**, R6256 (1997); *Phys. Soc. Jpn.* **66**, 3329 (1997).
 - [13] A. G. Rossberg, A. Hertrich, L. Kramer, and W. Pesch, *Phys. Rev. Lett.* **76**, 4729 (1996).
 - [14] N. Oikawa, Y. Hidaka, and S. Kai, *Phys. Rev. E* **70**, 066204 (2004).
 - [15] H. Richter, A. Buka, and I. Rehberg, *Mol. Cryst. Liq. Cryst.* **251**, 181 (1994).
 - [16] J.-H. Huh, Y. Hidaka, and S. Kai, *Phys. Rev. E* **58**, 7355 (1998).
 - [17] E. Plaut and W. Pesch, *Phys. Rev. E* **59**, 1747 (1999); A. Krekhov, B. Dressel, W. Pesch, V. Delev, and E. Batyrshin, *ibid.* **92**, 062510 (2015).
 - [18] J.-H. Huh, Y. Hidaka, Y. Yusuf, N. Eber, T. Toth-Katona, A. Buka, and S. Kai, *Mol. Cryst. Liq. Cryst.* **364**, 111 (2001).
 - [19] J.-H. Huh, Y. Yusuf, Y. Hidaka, and S. Kai, *Phys. Rev. E* **66**, 031705 (2002).
 - [20] M. Scheuring, L. Kramer, and J. Peinke, *Phys. Rev. E* **58**, 2018 (1998); H. Amm, R. Stannarius, and A. G. Rossberg, *Phys. D (Amsterdam, Neth.)* **126**, 171 (1999).
 - [21] T. Ishibashi, Z. Kuang, S. Yufune, T. Kawata, M. Oda, T. Tani, Y. Iimura, and K. Sato, *J. Appl. Phys.* **100**, 093903 (2006).

- [22] J.-H. Huh, Y. Hidaka, A. G. Rossberg, and S. Kai, *Phys. Rev. E* **61**, 2769 (2000).
- [23] E. Bodenschatz, W. Zimmermann, and L. Kramer, *J. Phys. (Paris)* **49**, 1875 (1988).
- [24] S. Kai and K. Hirakawa, *J. Phys. Soc. Jpn.* **40**, 301 (1976).
- [25] P. Petrescu and M. Giurgea, *Phys. Lett. A* **59**, 41 (1976).
- [26] S. Kai, W. Zimmermann, and M. Andoh, *Mod. Phys. Lett. B* **04**, 767 (1990).
- [27] S. Kai and W. Zimmermann, *Prog. Theor. Phys. Suppl.* **99**, 458 (1989).
- [28] J.-H. Huh, *J. Phys. Soc. Jpn.* **85**, 024002 (2016).
- [29] A. Joets, X. D. Yang, and R. Ribotta, *Phys. D (Amsterdam, Neth.)* **23**, 235 (1986); A. Joets and R. Ribotta, *J. Phys. (Paris)* **47**, 595 (1986).
- [30] A. Buka, T. Borzsonyi, N. Eber, and T. Toth-Katona, *Lect. Notes Phys.* **567**, 298 (2001).
- [31] S. Komineas, H. Zhao, and L. Kramer, *Phys. Rev. E* **67**, 031701 (2003).
- [32] S. Tatsumi, M. Sano, and A. G. Rossberg, *Phys. Rev. E* **73**, 011704 (2006).
- [33] E. Plaut, W. Decker, A. G. Rossberg, L. Kramer, W. Pesch, A. Belaidi, and R. Ribotta, *Phys. Rev. Lett.* **79**, 2367 (1997).
- [34] N. Oikawa, T. Gunji, and Y. Hidaka, *Phys. Rev. E* **101**, 062204 (2020); J. -H. Huh and H. Osoguchi, *ibid.* **101**, 062701 (2020).
- [35] G. J. Choi, J. M. Song, C. G. Jhun, J.-H. Huh, and J. S. Gwag, *Phys. Rev. E* **96**, 040701(R) (2017); D. G. Ryu, J.-H. Huh, Y.-K. Kim, and J. S. Gwag, *ibid.* **101**, 062703 (2020).
- [36] H. Yamazaki, S. Kai, and K. Hirakawa, *J. Phys. Soc. Jpn.* **52**, 1878 (1983).
- [37] S. Nasuno, O. Sasaki, S. Kai, and W. Zimmermann, *Phys. Rev. A* **46**, 4954 (1992).
- [38] M. Shiomi, E.-J. Choi, and J.-H. Huh, *Phys. Rev. E* **102**, 042704 (2020).
- [39] S. Kai, K. Yamaguchi, and K. Hirakawa, *Jpn. J. Appl. Phys.* **14**, 1653 (1975).
- [40] J.-H. Huh, A. Kuribayashi, and S. Kai, *Phys. Rev. E* **80**, 066304 (2009).
- [41] L. Nasts, A. Lupu, and M. Giurea, *Mol. Cryst. Liq. Cryst.* **71**, 65 (1981).
- [42] M. V. Mitrokhin, L. Johnsen, R. Fagerberg, C. Kristiansen, F. J. Farrand, K. H. Holm, R. Palm, K. Netland, and V. L. Aristov, *Mol. Cryst. Liq. Cryst.* **411**, 255 (2004).
- [43] B. Sunuwar, P. Katwal, T. Bhandari, N. Baizalee, B. Bhandari, and B. Pokharel, *GoldenGate J. Sci. Technol.* **3**, 1 (2017).
- [44] See Supplemental Material at <http://link.aps.org/supplemental/10.1103/PhysRevE.103.062701> for comparing flows of two instabilities: (a) PW at $V = 165$ V and $f = 1300$ Hz; (b) WD at $V = 6.5$ V and $f = 30$ Hz. The videos were recorded at 60 fps.